Cement & Concrete Composites 33 (2011) 966–977

Contents lists available at ScienceDirect

Cement & Concrete Composites

journal homepage: www.elsevier.com/locate/cemconcomp

Modeling of phase interfaces during pre-critical crack growth in concrete

D. Asahina [a], E.N. Landis [b], J.E. Bolander [a,*]

[a] Department of Civil and Environmental Engineering, University of California, Davis, One Shields Avenue, Davis, CA 95616-5294, USA
[b] Department of Civil and Environmental Engineering, University of Maine, 5711 Boardman Hall, Orono, ME 04469, USA

ARTICLE INFO

Article history:
Received 7 July 2010
Received in revised form 7 January 2011
Accepted 24 January 2011
Available online 1 February 2011

Keywords:
Pre-critical cracking
Lattice models
Phase interface
Meso-structure
X-ray microtomography
Image analysis

ABSTRACT

Recent developments in the Rigid-Body-Spring Network (RBSN) modeling of concrete are presented, with candid assessments of research needs for the modeling of pre-critical crack growth under multi-axial stress conditions. Fracture of micro-concrete specimens is investigated through the combined use of such discrete (lattice) models, X-ray tomography, and imaging techniques. The specimens contain small amounts (10–50 wt.% fraction) of spherical glass aggregates. Acid-etching of the glass aggregate surfaces is done to vary the bond properties of the matrix–aggregate interface. Tomographic images of the unloaded specimens provide the initial configurations of the three-dimensional lattice models, which are based on a three-phase representation of the material meso-structure: fine-grained mortar matrix, glass aggregate inclusions, and matrix–aggregate interfaces. The numerical and physical test results agree well with respect to peak loads and the associated crack patterns. Material structure and interface properties affect pre-critical cracking, in accordance with expectations. Dependence of composite strength on aggregate content and arrangement is studied through simulations of large sets of nominally identical models, which differ only in random positioning of the aggregates.

1. Introduction

Fracture processes in concrete typically involve the nucleation and/or growth of multiple defects, in contrast to conventional engineering fracture mechanics in which crack growth extends from a single, dominant crack. The debonding of aggregate inclusions at sub-critical load levels can be viewed as a source of defects, typically distributed throughout the material. The interaction and potential coalescence of these multiple cracks, as well as the interactions of this crack system with the various phase fractions, affect the morphology of the fracture surface and composite toughness [39].

Fig. 1 depicts typical load-deformation behavior of concrete under tension. Whereas the ultimate aim is to understand the complete load-deformation response of concrete materials, study of the pre-peak portion of the loading history also has merit. Many of the opportunities for engineering stronger and tougher composites are evident in the earlier stages of loading, where microcracks and other precursors to failure are developing. Pre-peak microcracking can significantly affect the transport properties of concrete materials, particularly for load levels approaching peak load [2]. Although the processes of such pre-critical cracking are understood in a qualitative sense, our abilities to quantitatively relate the material design variables and performance outcomes are still relatively weak. This weakness is significant, since improved understandings of fracture and the development of reliable predictive models ultimately depend on having accurate quantitative descriptions of fracture at the microstructural level.

The literature is populated with references to discrete models of concrete. The term *discrete modeling* is open to at least two interpretations: (1) the material structure (e.g. matrix, aggregates and matrix–aggregate interface) is explicitly represented by the model discretization, as was first done by Roelfstra et al. using finite elements [33]; and (2) the method relies on discontinuous approximations of the field variable(s) over the model domain, as in the use of 1-D lattice elements. Many models, including the approach described here, satisfy both interpretations [3,12,13,34,36,43].

Lattice models are capable of simulating the various field variables of interest for concrete materials (with no particular disadvantages relative to continuum approaches, when modeling temperature and humidity fields, for example). When modeling displacement fields, however, both advantages and disadvantages are apparent. As an advantage, the discrete form of lattice models more naturally represents the inherently discontinuous nature of cracking. For 3-D continuum approaches at least four nodes are involved in modeling the processes of material separation, whereas material separation involves only two lattice nodes (in a local sense) for the discrete approach . This greatly simplifies the modeling effort and strengthens our abilities to achieve traction-free conditions associated with a fully formed crack. Furthermore,

* Corresponding author. Tel.: +1 530 752 8226; fax: +1 530 752 7872.
E-mail address: jebolander@ucdavis.edu (J.E. Bolander).

0958-9465/$ - see front matter © 2011 Elsevier Ltd. All rights reserved.
doi:10.1016/j.cemconcomp.2011.01.007

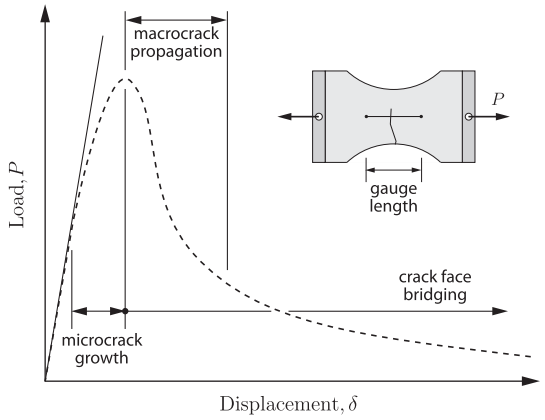

Fig. 1. Four-stage fracture model patterned after van Mier [38].

when approaching finer scales of observation, the material becomes progressively more discontinuous. The notion of a continuum no longer holds and a lattice-type structure is more appropriate. As one main disadvantage, the discontinuous, 1-D element approximation of the displacement field is currently unable to represent the Poisson effect in a local (intra-element) sense.

The development of lattice models has been motivated, at least in part, by the need to model inherently discontinuous phenomena that affect behavior at one or more length scales of a material. Along with the classical approaches described in Herrmann and Roux [16], a variety of lattice-type models have been developed to study fracture of disordered materials, including concrete [12,34,37,40]. The approach considered here is based on the Rigid-Body-Spring concept of Kawai [7,19].

To investigate pre-critical cracking and its effects on fracture development, we combine 3-D lattice models of fracture with high-resolution tomographic imaging of micro-concrete specimens under loading [23]. This paper first summarizes some recent developments of the Rigid-Body-Spring Network (RBSN) approach, with attention to fracture under multi-axial stress conditions. Thereafter, an experimental program is described in which micro-concrete (consisting of glass aggregates embedded within a fine-grained mortar matrix) is tested in the split-cylinder configuration. Properties of the matrix–inclusion interface are varied by acid-etching of the surfaces of the glass aggregates. A series of tomographic images for each micro-concrete specimen serve to define the initial configuration of each corresponding lattice model, and enable direct comparisons of 3-D crack development under loading. This close coupling between the models and experiments enables the study of material structure and its effects on pre-critical cracking and specimen strength. In most respects, the simulation results meet expectations: cracks initiate along the weak interfaces at low load levels, but do not propagate into the matrix until reaching peak load. Specimen strengths are dependent on material structure, even for the dilute concentrations of aggregates considered.

2. Modeling framework: Rigid-Body-Spring Networks

2.1. Domain and material feature discretization

As is common for lattice models, the material domain is discretized as a collection of two-node elements (Fig. 2). A three-step procedure is followed during model construction:

- introduction of nodal points within the material domain. The process involves a strategic placement of nodes to explicitly define material features, followed by semi-random placement of nodes to populate the homogeneous phases [43];

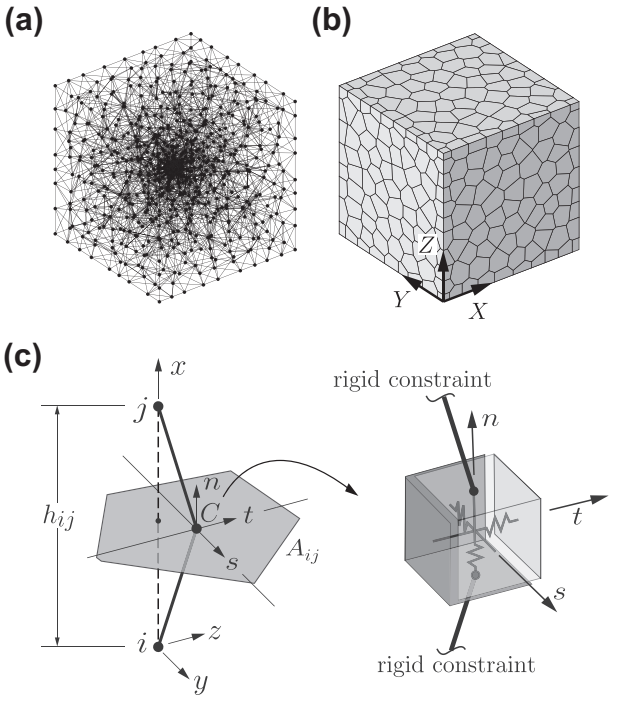

Fig. 2. Model construction: (a) Delaunay tessellation of a semi-random set of points; (b) dual Voronoi tessellation; and c) typical lattice element with a zero-size spring set located at centroid C of facet area A_{ij}.

- Delaunay tessellation of the nodal points [30], which defines the lattice topology; and
- construction of the dual Voronoi tessellation. The Voronoi cell facets define element properties, as described in the following section.

It is known that the properties of the matrix–aggregate interface can profoundly affect the mechanical and transport properties of concrete [39,41]. Therefore, this research differentiates between elements that represent: (1) main phases (e.g. aggregate or matrix), which are assumed to be homogeneous at the material meso-scale; and (2) phase interfaces. There is a practical minimum size of aggregate that can be discretized, considering available computational resources. If modeling of material variability at finer scales is desired, it can be done through the statistical assignment of properties [16].

For the modeling of homogeneous phases, the size, geometry and orientation of elements are randomly set, and have no relation to material structure. It follows that discretization of the homogeneous phases should not bias the model results. In contrast, elements representing phase interfaces are oriented normal to the interface. Element length (h_{ij} in Fig. 2) is adjustable and can approximate the small interface thicknesses common to cement-based composites. The matching of element orientation and size to phase interfaces facilitates the realistic modeling of those material features. This strategy also anticipates flow field calculations in which developing cracks, including interfacial cracking, are pathways that assist mass transport [14,18,29]. Details regarding the discretization of both convex and non-convex features are given elsewhere [5,42].

2.2. Model formulation and solution procedure

Each lattice element consists of a zero-size spring set that is connected to the lattice nodes by rigid-arm constraints. Each node has six degrees of freedom for the 3-D case. The spring set is

formed from three axial springs and three rotational springs (referenced to local coordinate axes $n-s-t$) as shown in Fig. 2c, in which the rotational springs have been omitted. The axial springs are assigned stiffness according to

$$k_s = k_t = \alpha_1 k_n = \alpha_1 \alpha_2 E \frac{A_{ij}}{h_{ij}} \tag{1}$$

in which E is elastic modulus and A_{ij} is the area of the Voronoi facet common to nodes i and j (Fig. 2c). By adjusting α_1 and α_2 in accordance with experimental results, macroscopic modeling of both elastic constants (E and Poisson ratio, ν) is possible. For the special case of $\alpha_1 = \alpha_2 = 1$, the zero-size spring set is rotationally invariant and the model is *elastically homogeneous*; however, the Poisson effect is not activated (i.e. $\nu = 0$) as shown later in Section 2.3. The six spring coefficients are placed in a diagonal matrix

$$\mathbf{D} = (1-\omega)\ \text{diag}\ [k_n, k_s, k_t, k_{\phi n}, k_{\phi s}, k_{\phi t}] \tag{2}$$

from which the element stiffness matrix can be formed [5,43]. Here, ω is a damage index that ranges from 0 (undamaged) to 1 (completely damaged) and subscript ϕ signifies the rotational spring terms. In the classical brittle lattice approach, ω is either 0 or 1. The structural stiffness matrix, which is stored in skyline form, is produced as an assemblage of the element stiffness matrices. Nodal displacements are obtained by solving the system equations using Crout elimination.

Forces and/or displacements are applied incrementally with equilibrium iterations in each increment. Following the convention of classical lattice models [17], only one element is allowed to break per iteration. For each element e within the model, a stress ratio of the form

$$\rho_e = \sigma_e / \hat{\sigma} \tag{3}$$

is calculated, where σ_e is a measure of stress acting within element e and $\hat{\sigma}$ is a strength defined by a limiting surface. The calculation of these terms depends on whether element e represents a homogeneous phase or a material interface, as described in Section 2.4. According to $\rho_c = \max(\rho_e) \geqslant 1$, the most critical element undergoes fracture, which entails a reduction of its elastic stiffness and an associated release of element forces. For the simulations that follow, incremental loads are applied by displacement control and load rate/duration effects are not considered. Additional details regarding the element formulations and solution procedure are given elsewhere [42].

2.3. Lattice modeling of the Poisson effect

There are significant differences in the local stress/force conditions within discrete and continuum models. For example, a regular network of truss elements under uniaxial compression contains opposing reactive elements (in diagonal compression or lateral tension, as shown in Fig. 3), whereas in homogeneous continua all normal stress components are either compressive or have zero magnitude. Lattice models have been used to simulate fracture under compressive loading and, in the absence of lateral restraint, tend to exhibit vertical cracking [35], as seen during laboratory testing. It can be argued that the combination of lateral tension and stress-based fracture criteria indirectly account for the origins of fracture, which reside in heterogeneity apparent at finer scales. However, such multi-scale views are not common.

Proper accounting of the Poisson effect is an issue for two-node (lattice-type) discretizations of continua [15,31]. As is commonly done for lattice models, macroscopic representation of the Poisson effect can be controlled by adjusting the elastic and geometric properties of the lattice elements. Macroscopic Poisson effect of the RBSN can be obtained by adjusting the values of α_1 and α_2 in Eq. (1). For example, consider the cubic domain in Fig. 2 under uniform compressive loading, σ. A Mohr's circle representation of the stress state at each lattice node can be plotted, as shown in Fig. 4, for the $n-t$ stress components. A similar result can be produced for the $n-s$ direction. For the case of $\alpha_1 = \alpha_2 = 1$, the model is elastically homogeneous, albeit with $\nu = 0$. A macroscopic Poisson ratio of $\nu = 0.17$, which is typical of non-saturated concrete, is achieved by setting $\alpha_1 = 0.32$ and $\alpha_2 = 1.56$. The stress pairs for this case, however, exhibit scatter about the theoretical solution. This scatter can be viewed as artificial heterogeneity, since it does not correspond to physical features of the material.

As a further check on model performance, relative errors of the nodal displacements for both cases are given in Table 1, where relative error is defined as

$$e_r = \frac{||u-u^h||_2}{||u||_2}, \quad ||u-u^h||_2 = \sqrt{\sum_{i=1}^{N} (u(\mathbf{X}_i) - u^h(\mathbf{X}_i))^2}, \tag{4}$$

in which $\|\cdot\|$ is the L_2 error norm; u and u^h are the exact and numerical solutions, respectively, in the axial (or lateral) directions at locations $\mathbf{X}$; and N is the total number of nodes. Here, too, the RBSN with ν=0 is elastically homogeneous under uniform modes of straining (to within algorithmic precision), whereas errors occur for the case where $\nu \neq 0$. Similar results have been reported before [8,42], but are revisited here due to the importance of the problem.

2.4. Fracture representation

As previously noted, two types of elements are used to model the composite material: (1) elements representing material features, such as the matrix–inclusion interface and (2) elements that represent main phases that are considered to be homogeneous at

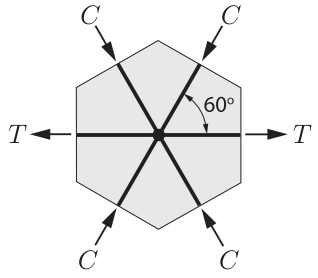

Fig. 3. Equilibrium of a unit cell of a triangular lattice network under vertical compression (C : compressive force; T : tensile force).

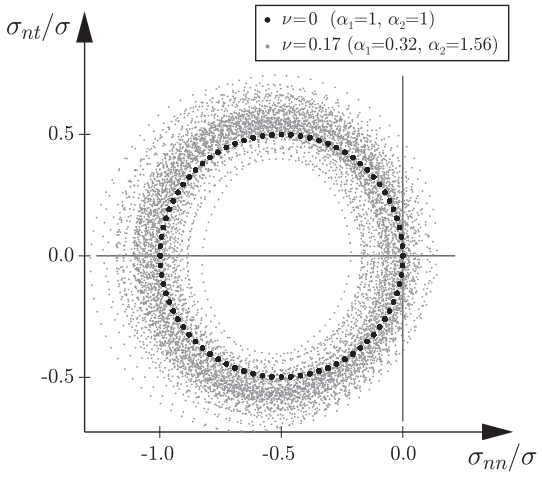

Fig. 4. Mohr's circle representation of stress state at lattice nodes under uniaxial compressive loading.

Table 1
Relative errors e_r in nodal displacements for uniaxial compressive loading.

Direction	RBSN ($\nu = 0$)	RBSN ($\nu = 0.17$)
Axial	9.5×10^{-9}	2.4×10^{-2}
Lateral	–	5.1×10^{-1}

the scale of interest. Accordingly, the fracture model associated with each element type is different, as described in the following sections.

2.4.1. Interface fracture

The irregular lattice modeling of these composite materials allows for a precise control over the orientation and thickness of the interfacial transition zone (ITZ) between the aggregate and matrix. This is in contrast to regular lattice models in which a constant element size is used to represent all aspects of the material structure. For the results that follow, the strength properties of the interface are defined by a Mohr-Coulomb surface with a tensile strength, f_n, cut-off as shown in Fig. 5. The surface is defined in terms of its inclination ψ with respect to the σ_{nn} axis and intercept with either shear axis, c. The normal and two shear stress measures are σ_{nI}=F_I/A_{ij}, where F represents a spring force and index I corresponds to each of the $n-s-t$ axes, respectively. The determination of the critical stress ratio ρ_c (Eq. (3)) involves the calculation of $\rho = \overline{OP}/\overline{OP_o}$ for each interface element, where $\overline{OP} = (\sigma_{nn}^2 + \sigma_{ns}^2 + \sigma_{nt}^2)^{0.5}$ and P_o is the point where $\overline{OP}$ intersects the Mohr-Coulomb surface (or the tension cut-off surface) as shown in Fig. 5.

At this stage in the model development, there is no option to soften the interface element or provide a frictional plateau for shear loading, even though test results indicate frictional resistance is maintained after interface strength is overcome in shear [1].

2.4.2. Fracture of homogeneous phases

The RBSN was first applied to modeling fracture driven by predominately tensile loading. For such cases, a vectorial representation of stress is sufficient. In Yip et al. [42], the forces in the uniaxial springs connecting two cells (at point C in Fig. 2c) are calculated for each iteration cycle. The resultant of this set of forces, $F_R = (F_n^2 + F_s^2 + F_t^2)^{0.5}$, is used to obtain a measure of tensile stress within each element

$$\sigma_R = \frac{F_R}{A_{ij}^P} \tag{5}$$

where A_{ij}^P is the projected area of A_{ij} on a plane perpendicular to F_R. This σ_R serves as σ_e in Eq. (3), whereas $\hat{\sigma}$ varies according to a tensile softening relation [4,5,9].

This uniaxial, vectorial stress approach to fracture within the RBSN is energy conserving and mesh insensitive for predominantly tensile stress fields [5,9]. However, complications arise when such uniaxial notions of stress are applied to modeling cases of multi-axial stress (e.g. the modeling of split-cylinder tests considered later in this paper.) For such loading situations, it is often the case that F_R is compressive in nature. One way to retain a simple vectorial representation of stress is to include the individual n (normal) and s, t (tangential) stress components within the fracture criterion, similar to the Mohr-Coulomb approach considered in the previous section. Indeed, this multi-component approach is common within other RBSN models of concrete materials. However, such an approach associates the random polyhedral geometries of the Voronoi diagram with actual material features, which is difficult to justify.

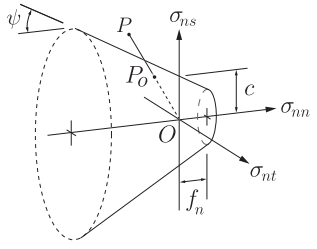

Fig. 5. Mohr-Coulomb surface with tension cut-off.

An alternative approach has been taken for the split-cylinder test simulations described later in this paper. The tensorial state of stress can be calculated at the lattice nodes by considering equilibrium of the spring forces of elements framing into a given node [8,42]. Whereas stress values at the nodes are useful for visualization purposes, intra-element stress values are needed for fracture simulation. Elemental stresses are calculated according to

$$\overline{\boldsymbol{\sigma}} = (\boldsymbol{\sigma}_i + \boldsymbol{\sigma}_j)/2 \tag{6}$$

where $\boldsymbol{\sigma}_i$ and $\boldsymbol{\sigma}_j$ are the stress tensors at neighboring nodes i and j, respectively. Maximum principal tensile stress, which is obtained from $\overline{\boldsymbol{\sigma}}$, serves as σ_e in Eq. (3). In this way, fracture under multi-axial stress conditions can be simulated. However, this approach does not readily account for the possibility of softening, since the nodal stresses are based on element forces framing into the nodes from all connected elements. Further developments are necessary.

3. Effects of interface heterogeneity on aggregate debonding

Consider the basic case of a spherical aggregate embedded within a homogeneous matrix under uniform (far-field) tension (Fig. 6a). The uniform tension condition is implemented by making the aggregate diameter d_a small relative to the cubic domain size of $100d_a$. The large size difference is not essential, but it illustrates the versatility of the meshing procedure [23]. The aggregate inclusion is assumed to be stiff relative to the matrix at a modular ratio of $E_a/E_m = 10$, where subscripts a and m denote the aggregate and matrix, respectively. Interface thickness has been set to $t_i = d_a/50$ for these simulations. As noted in Section 2.4.1, the breaking of interface elements is brittle and governed by a Mohr-Coulomb surface with a tension cut-off (Fig. 5).

Two types of (weak) interface were considered: one of uniform strength and the other of varying strength. For the latter case, the strength of interface elements was normally distributed about a mean value μ, which is equal to the strength assumed for the uniform case. A large coefficient of variation (of 50%) was used for the assignment of element strengths for the non-uniform case (Fig. 6b). At this stage of the investigation, the random assignment of strength is not spatially correlated.

With increasing loading, interface elements most directly aligned with the loading direction are the first to break, as shown in Fig. 6c for the case of uniform interface strength. Positioning of the corresponding fracture events in Mohr-Coulomb stress space signifies element breaking under nearly pure tension. Due to the sudden removal (brittle fracture) of the first of these elements, neighboring elements undergo fracture even without increasing the load point displacement. This unstable crack propagation, characterized by fracture events drifting from the fracture surface, is assisted by the lack of artificial heterogeneity in the interface modeling. By appropriately advancing/retracting load-point displacements, the fracture events can be held to the fracture surface. However, the sequencing of events is not altered and the depiction of events (in Fig. 6d) is arguably more descriptive of model behavior. As aggregate debonding continues, it is increasingly a tension-shear phenomenon. The fracture process eventually

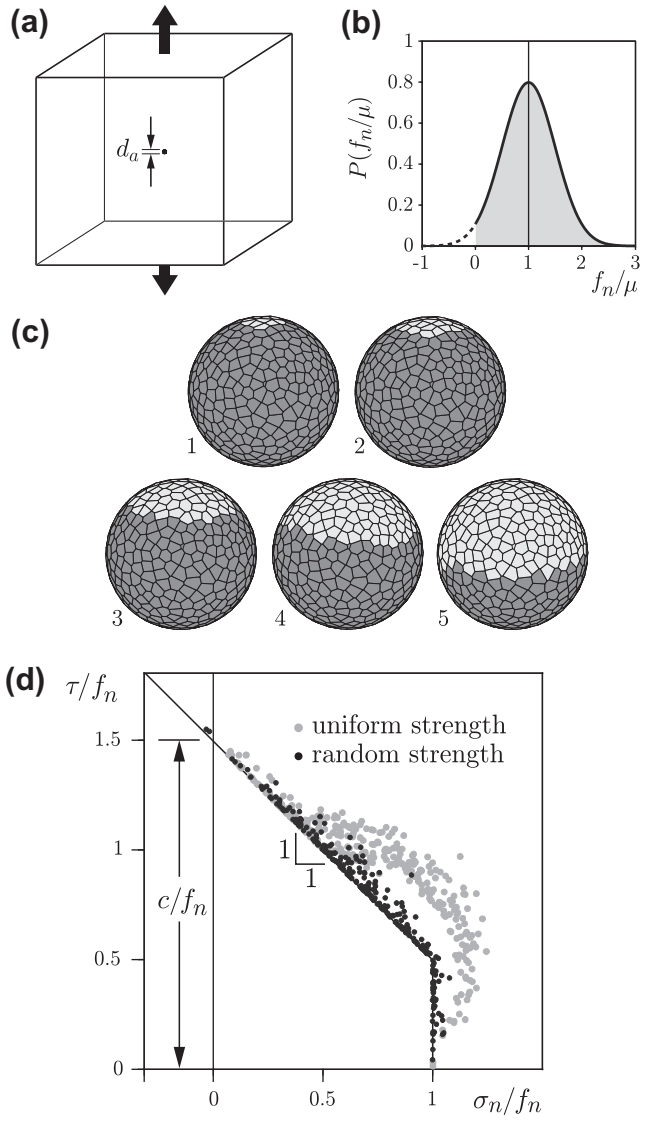

Fig. 6. (a) Spherical inclusion within a vertical tension field; (b) probabilistic assignment of interface element strength; (c) stages of inclusion debonding; and (d) distribution of fracture events about the fracture surface, where $\tau = (\sigma_{ns}^2 + \sigma_{nt}^2)^{0.5}$.

stabilizes, in the sense that small increases in load-point displacement do not produce bursts of element breakages.

The same tensile loading simulation is repeated for the second case, for which interface strength is randomly distributed. This statistical form of heterogeneity results in more stable fracture of the interface, as evidenced by movement of the bulk of the fracture events toward the fracture surface (Fig. 6d). From another perspective, load-point displacements can be gradually increased without the dramatic snap-back behavior seen from the uniform interface model. Similar forms of toughening have been produced by introducing heterogeneity within models of tensile fracture of cement composites, albeit at coarser resolutions of the material structure [40]. Future work will include study of how spatial correlation of the interface strength assignments affects fracture behavior.

4. Morphology-based simulation of micro-concrete fracture

Pre-critical cracking of micro-concrete, tested within the split-cylinder configuration, is studied through the combined use of the RBSN approach, high-resolution X-ray tomography and image analyses. Tomographic images of the micro-concrete cylinders -define material structure within the models, establishing a near one-to-one correspondence between the physical and numerical specimens at the meso-scale.

4.1. Experimental program

Characterization of concrete microstructure was carried out using X-ray tomography, a 3-D imaging technique that produces high-resolution spatial mappings of material morphology. For the work described here, synchrotron radiation provided the high flux, monochromatic X-ray source that is necessary to image the subtle variations between the different phases of the composite material. Tomographic images were reconstructed from 1500 through-transmission radiographs taken between 0° and 180°. The resulting volume images were nominally 1000 × 1000 × 1000 cubic voxels, each measuring 6 μm on a side.

Details of the experiments are described elsewhere [24], but are summarized here for completeness. A small loading frame was constructed such that applied load and resulting deformation could be monitored without interfering with the tomographic scan, which requires no parts move into or out of an image during rotation. The experimental protocol called for a preliminary scan of an undamaged specimen, with subsequent scans taken at progressively greater displacements of the load platen (Fig. 7). The goal was to scan specimens at two or more load levels prior to failure, but as peak load was not known *a priori*, this was not always achieved. A final scan was made after peak load. A split-cylinder configuration was chosen because of the relative ease in producing tensile fracture.

The specimens were produced using a conventional portland cement with a water-to-cement ratio $w/c = 0.40$. Fines (passing a No. 100 sieve) were added, along with spherical glass aggregates of nominal diameter $d_a = 0.5$ mm (Fig. 8). The spherical shape of the aggregates simplifies their discretization within the lattice model. To further facilitate modeling, the aggregates were distributed sparsely throughout the mix at a weight fraction of $W_a = 0.1$, which corresponds to a volume fraction $V_a = 0.078$. The specific gravity of the glass aggregate was measured to be 2.63.

Two specimen types were considered, which differed in pretreatment of the aggregate surfaces: aggregates with smooth (untreated) surfaces, and aggregates with rough acid-etched surfaces (Fig. 8). The etching with hydrofluoric acid was done to modify the bonding properties of the aggregates with the fine-grained mortar matrix. In addition, specimens without aggregates were produced to measure the fracture properties of the fine-grained mortar. Loading within the tomographic setup was done for four specimens containing etched aggregates (E-series), two specimens containing untreated aggregates (U-series), and four fine-grained mortar specimens. Access to the test facilities was limited, which restricted the number of specimens that could be considered. The parametric study of the micro-concrete was limited to the surface conditions of the glass aggregates.

The material used in this study was cast in small blocks, which were then cured in a wet room for at least 28 days. The 5 mm diameter specimens were cored from the block and cut into disks nominally 3.5 mm long. The small specimen size was chosen to match that of the X-ray beam, and also monitor cracking at a 10 μm scale. The casting direction coincided with the cylinder axis. This reduces concerns regarding potential bleeding of the mix water and its effects on the highly stressed regions of the matrix–aggregate interface during split-cylinder testing.

The 3-D image analyses consisted of several steps, the first of which was to isolate and locate the position of the aggregates in the unloaded specimen. Aggregates were identified in the tomographic images by using a spatial standard deviation-based segmentation approach. A conventional intensity-based segmentation could not be used because the X-ray absorption characteristics

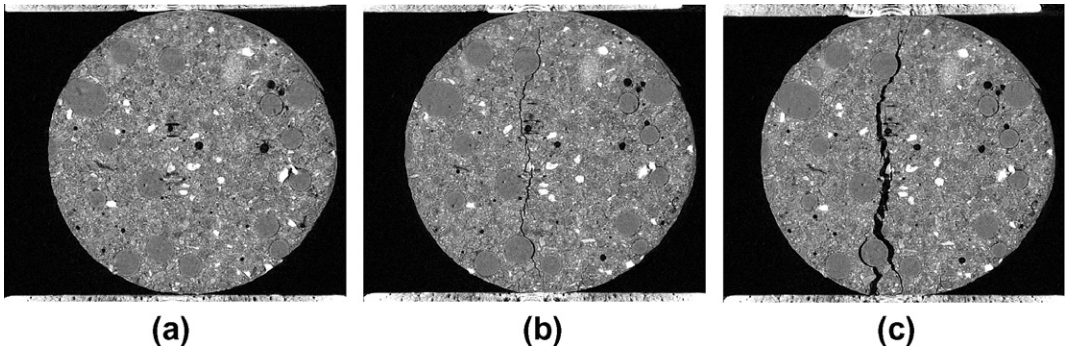

Fig. 7. Images of a cylinder section: (a) unloaded; (b) just prior to peak load; and (c) after peak load.

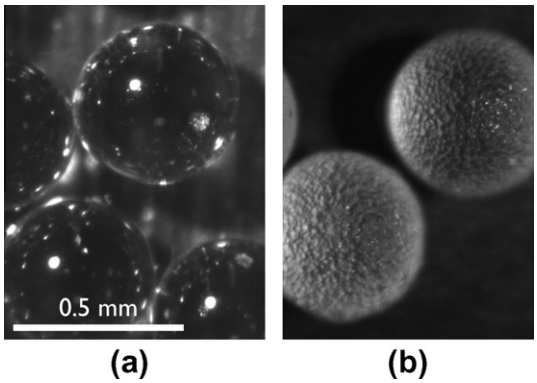

Fig. 8. (a) Untreated and (b) acid-etched-glass aggregates used as micro-concrete inclusions.

of the glass aggregates are similar to those of portland cement. However, because the aggregate composition is highly uniform compared to that of the cement matrix, we could identify aggregates by calculating the standard deviation of the intensities (brightness) of a $5 \times 5 \times 5$ voxel array surrounding each voxel. Within the aggregates, this standard deviation is quite low compared to that of the surrounding matrix. A cross-section of this processing is illustrated in Fig. 9. The segmented 3-D image of the glass aggregates is shown in Fig. 10a. Once the aggregates are identified, their centroids can be located and their effective diameters can be measured for use in a matched lattice model.

4.2. Model description and calibration

Micro-concrete specimens are discretized as shown in Fig. 10b, where the sizes and locations of the glass aggregate inclusions are obtained from the 3-D tomographic analyses. Each glass aggregate is thus identified and represented by its volume and the (X,Y,Z) coordinates of its centroid. In close agreement with the test specimens, the volume of each aggregate is represented as a sphere. For comparison, Man and van Mier [27,28] map X-ray tomographic data directly onto a lattice structure to obtain high-resolution discretizations of actual concrete aggregates, which are irregular in shape and possess non-convex features. Their use of basalt and marble aggregates, which are significantly denser than the cement-based matrix, heightened the contrast of phases within the tomographic images and therefore facilitated the phase identification.

Element types are assigned according to a three-phase representation of the micro-concrete: fine-grained mortar matrix, glass aggregate inclusions, and the matrix–aggregate interfaces. As explained earlier in this paper, the fracture criterion depends on element type. For the homogeneous phases (matrix and aggregate), fracture depends on maximum principal stress, obtained from the stress tensor given by Eq. (6), and a tensile strength limit (Section 2.4.2). For the phase interfaces, fracture is based on a multi-component vectorial measure of stress, limited by a Mohr-Coulomb surface with a tension cut-off (Section 2.4.1). To maintain elastic uniformity of the homogeneous phases, $\alpha_1 = \alpha_2 = 1.0$, which results in $\nu = 0$.

Incremental loading is applied along three arrays of nodes that run across the top and bottom of the specimen. Neither the nonlinear contact conditions nor friction along the contact surface are considered in these simulations. To reduce computational cost, half of each cylinder specimen in the longitudinal direction is modeled. Furthermore, inclusions outside of the assumed loading path (i.e. outside of the interval $-1 \leqslant X \leqslant 1$ mm), and those close to the cylinder boundary, have not been discretized. A typical numerical specimen consisted of about 13,000 nodes (which equates to roughly 80,000 degrees of freedom).

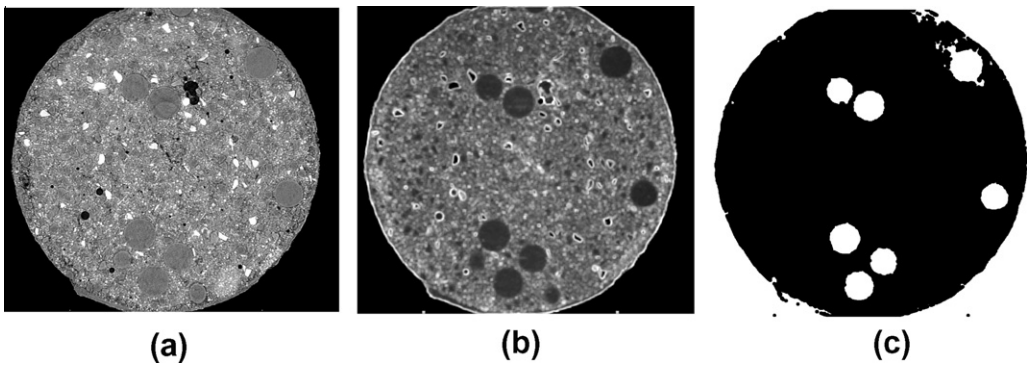

Fig. 9. Glass aggregate identification: (a) Raw data image; (b) regions of low standard deviation of voxel intensities; and (c) binary image highlighting of aggregates.

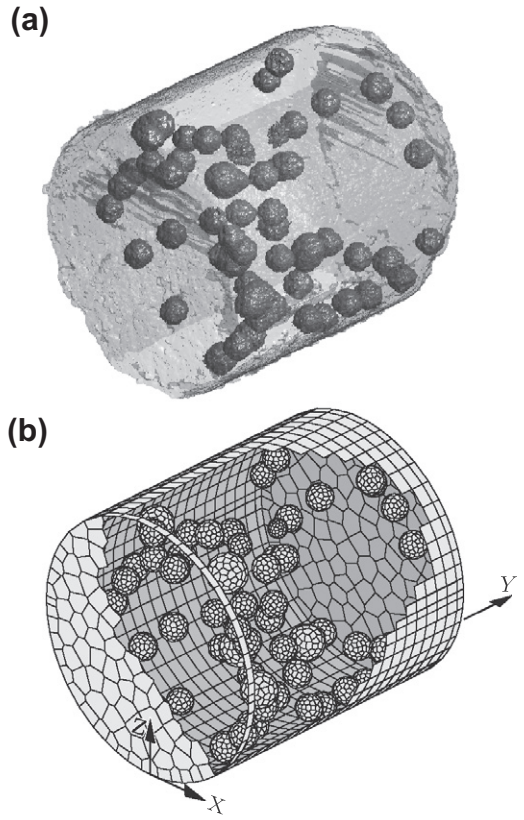

Fig. 10. (a) Tomographic image and (b) Voronoi discretization of split-cylinder specimen.

A numerical model was constructed for each of the specimens containing aggregates, except for one of the E-series specimens that exhibited abnormal behavior during physical testing. Apart from the classification of matrix–aggregate interface properties, these models differed only in the positioning of aggregate inclusions within specimens. Modulus of elasticity and tensile strength of the matrix were determined to be 8 GPa and 12 MPa, respectively, by calibrating the lattice model results (without inclusions) to the average response of the fine-grained mortar specimens. A reduced modulus of elasticity was used for the elements meeting the contact points to account for local effects. As a check, comparison was made with the well-known relation for estimating tensile stress from split-cylinder test results, i.e.

$$f = \frac{2P}{\pi bd} \tag{7}$$

where b and d are the width and diameter of the split-cylinder specimen, respectively, and P is the applied load. For the average peak load of the fine-grained mortar specimens, Eq. (7) gives f_m = 11.8 MPa, which is close to the calibrated value.

As noted in Section 3, each Voronoi polygon tiling a spherical inclusion corresponds to an interface element (Fig. 10b). Interface thickness was set to t_i = 10 μm, which is approximately $d_a/50$. Observations of the tomographic images did not justify larger values of interface thickness. Post-test study of the fracture surfaces indicated better bonding of the etched-glass surfaces compared to that of the untreated glass. Small portions of the matrix were attached to the etched-glass surface, whereas interface fracture alongside the untreated glass produced smooth surfaces. Tensile strength of the interface was assumed to be half that of the matrix for the case of etched-glass (i.e. f_i/f_m = 0.5) and yet half of that for case of untreated glass (i.e. f_i/f_m = 0.25). As explained later, the precise setting of these values did not appreciably affect the specimen strengths. Elastic modulus of the interface was set equal to that of the matrix. Elastic modulus and strength of the glass aggregates were set to 70 GPa and 33 MPa, respectively, as reported in the literature.

4.3. Simulation results and discussions

4.3.1. Cracking patterns

Several stages of pre-critical crack development appear within the split-cylinder test models (Fig. 11). Fracture initiates along regions of the matrix–aggregate interface that are more centrally located within the specimen. The load at which this occurs depends on the strength of the interface. Increasing interface strength, as intended by acid-etching of the glass aggregate surfaces, increases the loads over which interface cracking occurs. With increasing load, debonding along the interface continues, but fracture does not extend far into the matrix material until reaching peak load. These tendencies are studied in more detail in Section 4.3.4. Traversing peak load, matrix cracks join and ultimately extend across the height of the specimen. There is no evidence of cracking within the glass aggregates.

Cross-sections of the fractured specimens are compared in Fig. 12. Here, too, it is seen that cracks tend to go around the aggregates. Agreement between the cracking patterns is quite good, although this high degree of correspondence is not seen for many of the cross-sections. In the physical tests, fairly straight vertical cracks propagate through the matrix phase, whereas the crack patterns of the numerical model appear to be more tortuous. This difference is due, in part, to the graphical portrayal of the fracture surface, which depicts cracking along Voronoi cell boundaries. It appears that cracking direction is aligned with the element local coordinate system, but this is generally not the case, as described in Section 2.4.2. The secondary cracking near the supports is roughly captured in some of the models. It is anticipated that finer discretization and more realistic representation of the boundary conditions at the load platens will improve the model in that

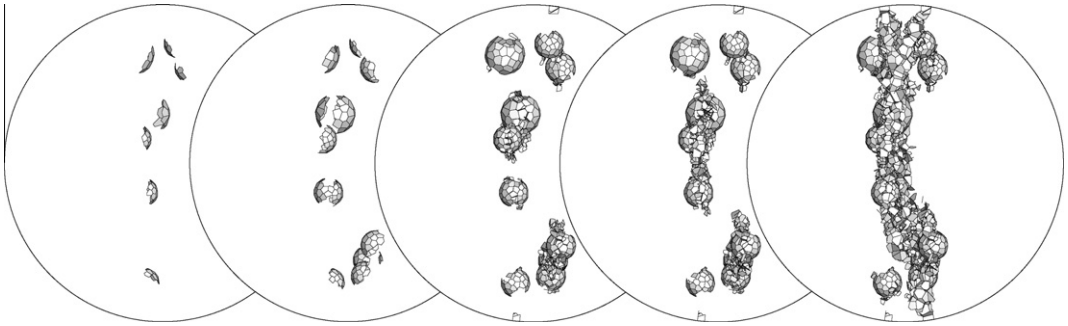

Fig. 11. Frontal view of 3-D fracture sequence.

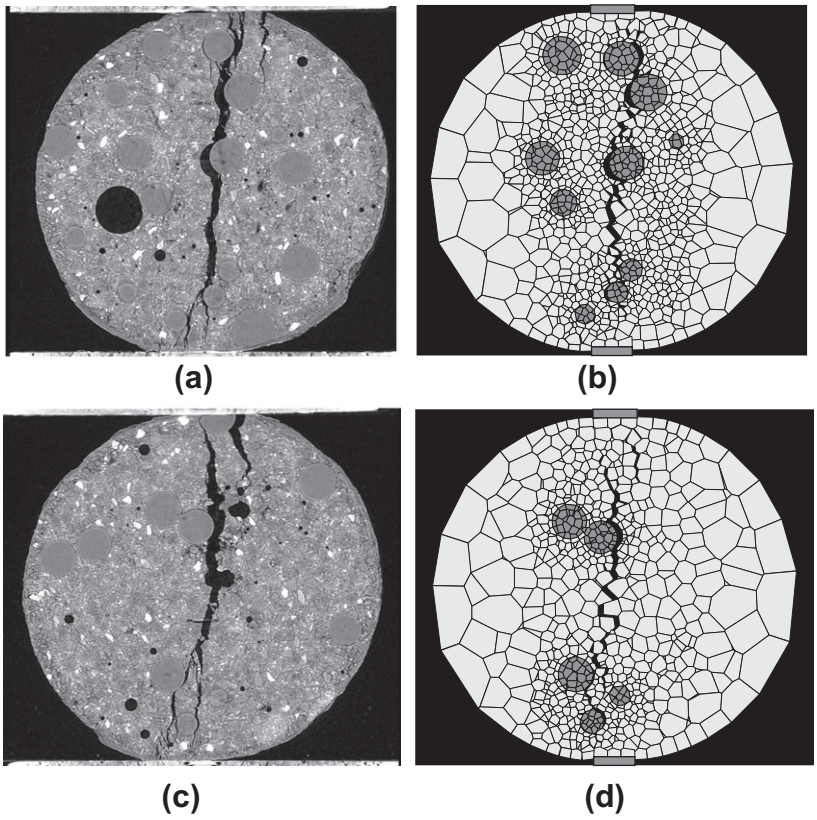

Fig. 12. Typical post-peak damage patterns: (a, c) tomographic images; and (b, d) lattice model results.

region. The high-resolution of cracking in the tomographic images enables accurate calculations of crack surface area and crack branching [21,22]. Finer discretization throughout the model domain would enable consideration of such finer scale features and their statistics, and a larger range of aggregate sizes when modeling ordinary concrete materials. Through effective utilization of computing technologies, more realistic structures can be discretized, as seen in the recent work of Man and van Mier [27,28].

4.3.2. Load–displacement patterns

Fig. 13 compares experimental and simulated load–displacement curves for each type of glass aggregate surface. The initial stage of the experimental curves exhibits hardening behavior that is typically associated with the nonlinear contact conditions between the circular cross-section and the planar load platens. Tomographic sections adjacent to the platens, in the $X-Y$ plane, also revealed non-uniform contact conditions due to irregularities in cylinder geometry, which likely contributed to this hardening behavior. In plotting the experimental curves, the start of each curve is offset so that a tangent to the linear portion of the curve (at higher loads) passes back through the origin. As matrix stiffness and strength were calibrated with an independent data set, these simulation results are predictions, at least to some degree.

The fine-grained mortar specimens used for calibration had an average peak load of 360 N. The average peak loads of the test specimens with unetched and etched aggregates were 230 N and

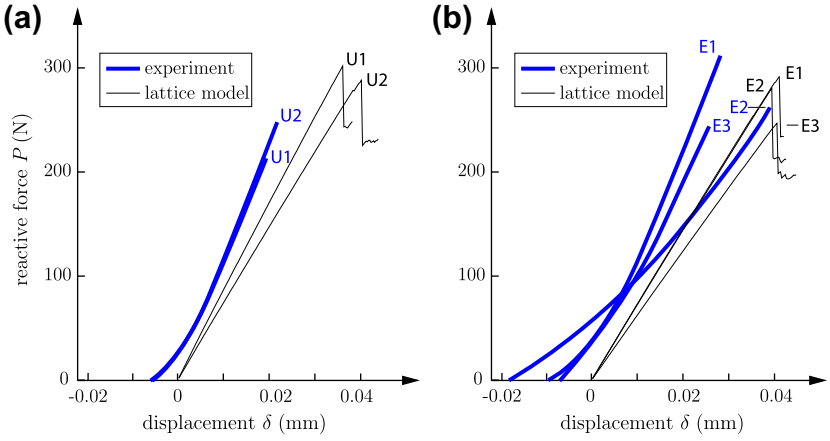

Fig. 13. Load–displacement response of split-cylinder specimens: (a) unetched-glass aggregates and (b) etched-glass aggregates.

272 N, respectively. The corresponding average strengths of their numerical counterparts were 294 N and 273 N. It is clear that adding the aggregates caused a similar loss of strength in both the experimental and numerical specimens. This tendency has been seen in other studies of interface fracture [25,26]. Following the abrupt drop in load after peak, residual load capacity remains fairly constant for a significant range of displacement, δ, as measured in other split-cylinder load tests [25].

Looking at the load–displacement results for the etched aggregate specimens, there appears to be a correlation between material structure and peak load, since material structure is the only potential source of variability in the numerical model. However, this tendency was not seen for the unetched aggregate specimens. For both types of specimens, debonding within the models had matured at relatively low load levels, so it is difficult to justify interfacial strength f_i as a primary factor on specimen strength, at least not for the low aggregate contents considered. Lilliu [25] and Lilliu and van Mier [26] used 3-D lattice models to study the relationship between concrete tensile strength, f_{tc}, and volumetric fraction of aggregates V_a ranging between 34% and 62%. Their simulations assumed $f_i/f_m = 1$ (or 0.25), which corresponds to strong (or weak) interfaces. For these two cases of interface strength, the difference in composite strength clearly diminished as the volume fraction of aggregates is reduced. For the small amount of aggregates ($V_a = 0.078$) used to obtain the results in Fig. 13, one expects interface strength to have little effect on composite tensile strength.

4.3.3. Assessment of specimen strength variation

The direct comparisons of numerical and physical specimens, as shown in Fig. 13, have served to partially validate the modeling approach. As a next step, the model has been used to explore potential scatter in peak load due to: (1) random variations in the positions of the glass aggregates; and (2) changes in aggregate content.

Table 2 presents the mean values μ and standard deviations σ of computed strength, f_{tc}, which have been normalized by the average test strength of the fine-grained mortar, $f_m = 11.8$ MPa. Each strength value in the table was obtained from N nominally identical specimens, which differ only in the positioning of aggregate inclusions. For each $W_a \neq 0$, the same N specimens were considered at the two different interface strengths. The corresponding frequency distributions of specimen strength, for the case of the stronger interface (E-series), are shown in Fig. 14. The frequency distribution plots for the weaker interface (U-series) are similar in appearance.

Table 2
Mean values and standard deviations of strength for nominally identical models of split-cylinder specimens.

W_a	N	$f_i/f_m = 0.25$ μ (σ)*	$f_i/f_m = 0.5$ μ (σ)*	Mean strength difference (%)
0	25	0.997 (0.00368)**	0.997 (0.00368)**	–
0.1	100	0.725 (0.0340)	0.731 (0.0316)	0.828
0.2	100	0.647 (0.0306)	0.660 (0.0283)	2.01
0.3	100	0.594 (0.0254)	0.610 (0.0246)	2.69

* μ (σ) is the mean value (standard deviation) of f_{tc}/f_m for N specimens.
** Matrix strength was calibrated for the case of $W_a = 0$. This set of model specimens does not contain the interface phase.

For the E-series, the mean strength of the model specimens with $W_a = 0.1$ agrees well with the experimentally determined mean strength, μ_{exp}, as seen in Fig. 14a. Such close agreement was not obtained for the U-series. For both cases, mean strength provided by the model decreases with increasing aggregate content. Analyses of the model results indicates that the reduction in strength is attributable to two mechanisms: (1) stress concentrations caused by the mismatch in elastic modulus between the matrix and inclusions; and (2) loss of resisting cross-section area due to debonding along the matrix–inclusion interfaces. The trend toward lower strength with increasing aggregate content agrees well with that seen in the numerical experiments of Lilliu [25] and Lilliu and van Mier [26].

For the case of the fine-grained matrix, without glass aggregates and assumed to be homogeneous, mean strength matches the theoretical strength (as a result of calibration), but exhibits practically no scatter (Table 2). For 25 numerical specimens, differing only in random discretization of the matrix, the coefficient of variation of split-cylinder strength is only 0.00369. This ability of the fracture model, implemented within an irregular lattice model of a continuum, to remove mesh bias from the solution is a noteworthy outcome of this research.

In Fig. 15, model results presented in Table 2 are compared with a different, earlier set of experimental results, obtained from specimens with $W_a = 0$, 0.1 and 0.5. Since both untreated and acid-etched-glass aggregates were considered in these earlier tests, the test specimens are designated as U-series and E-series, respectively. A total of 12 fine-grained mortar specimens were tested. At $W_a = 0.1$ (and 0.5), totals of 13 (and 8) specimens and 9 (and 8) specimens were tested for the U- and E-series, respectively. Peak loads were accurately recorded during the experiments, but displacement measurements were affected by a faulty sensor. In addition to the E-series results from Table 2, models were constructed for ten nominally identical specimens containing $W_a = 0.5$ of acid-etched aggregates. Results for the U-series model specimens differ little from those of their E-series counterparts (Table 2) and therefore are not plotted in Fig. 15 to avoid congestion. The following observations can be made:

- The physical and numerical test results agree well for all tested/simulated amounts of glass aggregates. Only the strength and stiffness of the matrix were calibrated, whereas the other quantities were obtained from the literature. The numerical results for $W_a \neq 0$ can be viewed as predictions.

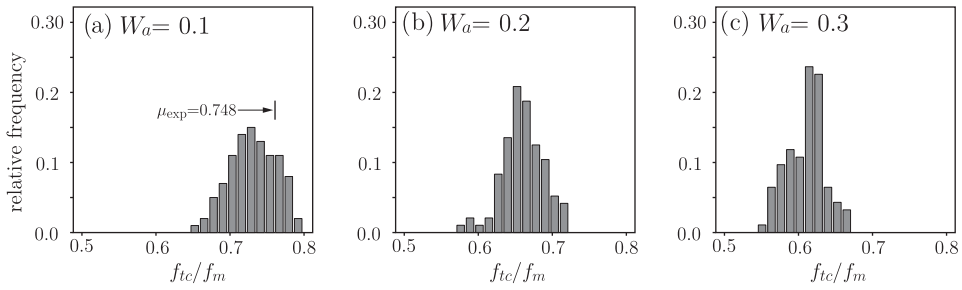

Fig. 14. Frequency distributions of normalized strength based on 100 nominally identical models differing only in random placement of E-series aggregates.

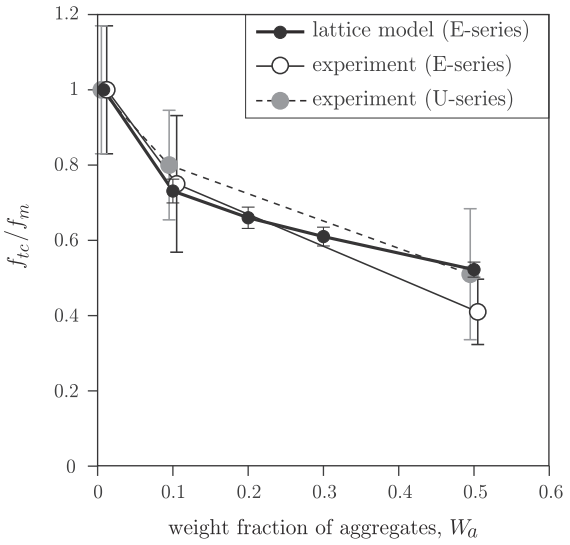

Fig. 15. Normalized strength for different weight fractions of aggregate. (The error bars indicate one standard deviation about the mean strength values).

- The variation of strength for the numerical models is significantly smaller than that observed in the physical tests. This is reasonable considering, in addition to the positioning of the glass aggregates, other potential sources of variability in the physical tests, such as differences in specimen size and geometry, unevenness along the loading surfaces, and the presence of some large air voids. Potential sources of variability in the models are limited to the random positioning of the glass aggregates and some minor degree of mesh bias. Similar studies have been conducted to study the effects of fiber distribution on the fracture behavior of fiber-reinforced cement composites [10].

4.3.4. Characterization of pre-critical cracking: model results

Process of pre-peak microcracking is studied along with its effect on specimen strength. Fig. 16 shows number of fracture events (i.e. element breakages) as a function of load on models of the split-cylinder specimens. Each plot is produced from the average of 100 specimens, whose peak loads are studied in Section 4.3.3. Results are provided for the event count of each element type, interface and matrix, and for their sum. Two scales are given for the horizontal axis. One corresponds to the previous cases (Fig. 14 and 15) in which the load value is normalized by the experimental mean strength for the fine-grained mortar, f_m. For the other scale, load is normalized by the mean specimen strength, f_{tc}, for that set of 100 specimens and, therefore, peak load occurs when this normalized value approaches unity. To reduce the computational cost associated with these Monte Carlo-type simulations, the post-peak portion of the load–displacement curve was not simulated. For this reason, the event counts associated with peak load have not been plotted in the Fig. 16. Several observations can be made:

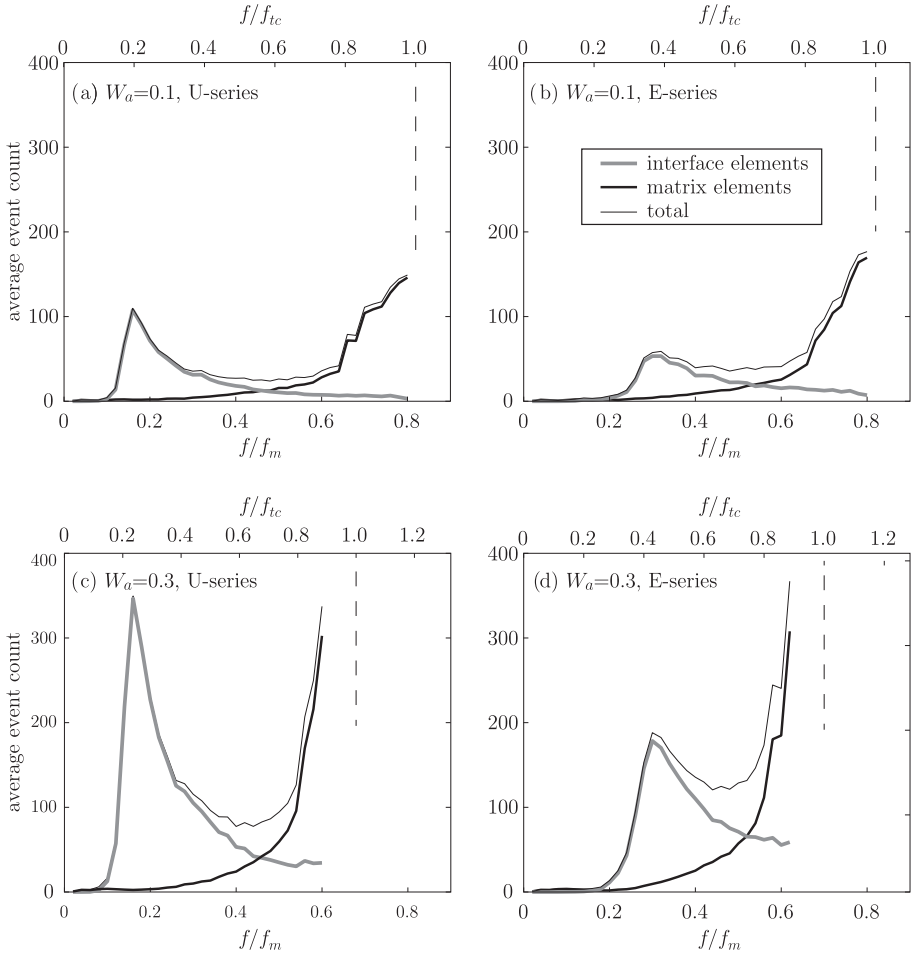

Fig. 16. Average fracture event counts during loading until near peak load (based on 100 random realizations of the micro-concrete specimens). The broken lines indicate average peak load.

- Interface fracture occurs more frequently at lower load levels, whereas fracture of the matrix becomes more prevalent when approaching peak load.
- The load levels at which interface fracture commences, and reaches a maximum, are proportional to the interface strength.
- Fracture event counts increase with increasing weight fraction of aggregates due, in part, to the higher number of interface elements.
- The peak associated with interface fracture is higher and sharper for the case of weaker interfaces.

As noted above, the event counts associated with matrix fracture dramatically increase when approaching peak load (Fig. 16). A similar trend is seen in the Acoustic Emission (AE) testing of concrete materials [20,32]. However, AE test results have not exhibited the well-defined peaks in event count at lower load levels, which are associated with interface cracking in the model. The modeling assumption of a constant value for interface strength likely contributes to the sharpness of these peaks in interface fracture events. The random assignment of interface strength, as described in Section 3, would reduce peak sharpness. Furthermore, such diffuse microcracking tends to consume much less energy than the matrix cracking that occurs during fracture localization [6,11]. It is possible that many of these lower energy events were not detected, or at least not counted, in previous AE studies.

5. Conclusions

This paper reports on the combined use of three-dimensional lattice models and high-resolution tomographic imaging techniques to study pre-critical cracking in concrete materials. To the extent possible, a one-to-one correspondence has been made between coarse-grained material structures of the numerical and physical experiments. Model results are compared with 3-D maps of internal damage and crack growth provided by *in situ* load testing of split-cylinder micro-concrete specimens within the tomographic setup. The following conclusions can be made regarding recent developments of the model and its application to simulating the experiments:

(1) Previous applications of the RBSN approach have shown that fracture criteria based on uniaxial, vectorial measures of stress are effective in simulating cracking under predominantly tensile loading. However, such approaches are inappropriate for multi-axial stress conditions, such as those prevailing within the split-cylinder test specimens considered in this study. To address this issue, the fracture criterion for each homogeneous material phase is based on tensorial measures of stress computed at the lattice nodes. Although the current implementation is limited to brittle fracture, and therefore model objectivity is an issue, good general agreement with the experimental crack patterns is obtained for the split-cylinder tests.

(2) For a spherical inclusion embedded within a matrix under uniform (far-field) tension, interface fracture transitions from a mode-I to a mixed-mode process. Interface fracture is markedly brittle when considering brittle interface elements of uniform strength. A cascading effect is observed, in which fracture events gradually drift from the fracture surface (even when holding the load-point displacements constant). The fracture process is significantly toughened through statistical variation of interface strength. Although the breaking of individual elements is brittle, the breaking process is quasi-stable in that load-point displacements can be progressively increased without significant snap-back behavior.

(3) Fracture of matrix–aggregate interfaces is governed by a multi-component vectorial representation of stress defined in coordinates local to the interface. The numerical model indicates cracking initiates along the matrix–inclusion interfaces at load levels proportional to interface strength. Crack propagation into the matrix, and the coalescence of these matrix cracks into a failure surface, occurs just prior to peak load. Since tomographic scans were conducted only at several stages of the loading history, the sequence of individual fracture events is not traced. It is particularly difficult to obtain images of matrix cracking just prior to peak load, since the peak load is not known *a priori*.

(4) Load tests of specimens without glass aggregate inclusions were used to calibrate the matrix properties for the simulations. The experimental and numerical specimens exhibited a similar loss of strength due to the addition of the glass aggregate inclusions. According to the model, strength loss is attributable to two mechanisms: (1) stress concentrations caused by the mismatch in elastic modulus between the matrix and inclusions; and (2) loss of resisting cross-section area due to debonding along the matrix–inclusion interfaces.

(5) The effects of aggregate content and positioning on peak strength have been studied by simulating multiple, nominally identical specimens differing only in those respects. These simulations are particularly useful in studying the sources of strength variability. The model indicates that the arrangement of inclusions affects peak load, although additional factors (e.g. irregularities of specimen geometry) appear to be more influential in causing scatter in the experimental results.

(6) Pre-critical microcracking has been characterized by counting fracture events within the models specimens. Interface fracture events exhibit an early peak, followed by a growing count of matrix fracture events leading up to peak load. The assumption of uniform interface strength contributes to the sharpness of the early peak. Introducing interface heterogeneity (possibly through the random assignment of interface strength considered earlier in this paper) would broaden the distribution of pre-peak fracture events. Further work is needed in correlating the numerically obtained fracture event counts with acoustic emission test results, particularly for the low energy events associated with interface debonding.

The good agreement between the experimental and numerical results (with respect to peak loads and ultimate crack patterns of the micro-concrete specimens) is notable, especially when considering the difficulties in conducting such small scale tests. The experimental and numerical approaches are complimentary in the type of information each provides. X-ray microtomography provides high-resolution 3-D pictures of material structure and cracking at distinct stages of the loading history. A wealth of information can be extracted from the tomographic data and image analyses, including various measures and statistics of cracking. Although the coarse domain discretizations considered in this paper do not resolve such fine-scale features, the models provide a continuous event-by-event description of the 3-D fracture process and thus insight into the cause-and-effect relationships that determine material performance and failure. The potential for quantitative simulation of pre-critical cracking can be more fully realized through improvements in these discrete (lattice-type) models of the material phases and their interfaces, model validation through comparisons with measurements of both global and fine-scale behaviors, and the effective utilization of emerging computing technologies.

Acknowledgement

The authors gratefully acknowledge the support of a collaborative grant from the US National Science Foundation (0625030 and 0625593).

References

[1] Aquino MJ, Li Z, Shah SP. Mechanical properties of the aggregate and cement interface. Adv Cement Based Mater 1995;2:211–23.
[2] Hoseini M, Bindiganavile V, Banthia N. The effect of mechanical stress on permeability of concrete: a review. Cement Concrete Compos 2009;31(4):213–20.
[3] Bažant ZP, Tabbara MR, Kazemi MT, Pijaudier-Cabot G. Random particle model for fracture of aggregate or fiber composites. J Eng Mech 1990;116(8):1686–705.
[4] Bažant ZP, Oh B-H. Crack band theory for fracture of concrete. Mater Struct 1983;16:155–77.
[5] Berton S, Bolander JE. Crack band modeling of fracture in irregular lattices. Comput Methods Appl Mech Eng 2006;195(52):7172–81.
[6] Bolander JE, Hikosaka H, He W-J. Fracture in concrete specimens of differing scale. Eng Comput 1998;15(8):1094–116.
[7] Bolander JE, Saito S. Fracture analyses using spring networks with random geometry. Eng Fract Mech 1998;61:569–91.
[8] Bolander JE, Moriizumi K, Kunieda M, Yip M. Rigid-Body-Spring Network modeling of cement-based composites. In: de Borst R, Mazars J, Pijaudier-Cabot G, van Mier JGM, editors. Fracture mechanics of concrete structures, la-FraMCos; 2001. p. 773–80.
[9] Bolander JE, Sukumar N. Irregular lattice model for quasistatic crack propagation. Phys Rev B 2005;71:094106. 12 pages.
[10] Bolander JE, Choi S, Duddukuri SR. Fracture of fiber-reinforced cement composites: effects of fiber dispersion. Int J Fract 2008;154:73–86.
[11] Cedolin L, Dei Poli S, Iori I. Tensile behavior of concrete. J Eng Mech 1987;113(3):431–49.
[12] Cusatis G, Bažant ZP, Cedolin L. Confinement-shear lattice model for concrete damage in tension and compression: I. Theory. J Eng Mech 2003;129(12):1439–48.
[13] Cusatis G, Bažant ZP, Cedolin L. Confinement-shear lattice model for concrete damage in tension and compression: II. Computation and validation. J Eng Mech 2003;129(12):1449–58.
[14] Grassl PA. A lattice approach to model flow in cracked concrete. Cement Concrete Compos 2009;31(7):454–60.
[15] Griffiths DV, Mustoe GGW. Modelling of elastic continua using a grillage of structural elements based on discrete element concepts. Int J Numer Methods Eng 2001;50:1759–75.
[16] Herrmann HJ, Roux S, editors. Statistical Models for the Fracture of Disordered Media. The Netherlands: Elsevier/North Holland, Amsterdam; 1990. 353 pp..
[17] Herrmann HJ, Roux S. Modelization of fracture in disordered systems. In: Herrmann HJ, Roux S, editors. tatistical models for the fracture of disordered media. Amsterdam (The Netherlands): Elsevier/North Holland;1990. p. 159–88.
[18] Idiart AE, López CM, Carol I. Modeling of drying shrinkage of concrete specimens at the meso-level. Mater Struct; 2010, doi:10.1617/s11527-010-9636-2.
[19] Kawai T. New discrete models and their application to seismic response analysis of structures. Nucl Eng Des 1978;48:207–29.
[20] Landis EN. Micro–macro fracture relationships and acoustic emissions in concrete. Constr Build Mater 1999;13:65–72.
[21] Landis EN, Nagy EN, Keane DT. Microstructure and fracture in three dimensions. Eng Fract Mech 2003;70(7-8):911–25.
[22] Landis EN, Zhang T, Nagy EN, Nagy G, Franklin WR. Cracking, damage and fracture in four dimensions. Mater Struct 2007;40(4):357–64.
[23] Landis EN, Bolander JE. Explicit representation of physical processes in concrete fracture. J Phys D: Appl Phys 2009;42(21):214002. 17pp.
[24] Landis EN, deWolski SC, Trainor KJ, Bolander JE. 3D in situ imaging of split cylinder fracture in model concrete, submitted for publication.
[25] Lilliu G. 3D analysis of fracture processes in concrete, Ph.D. Thesis. Delft University of Technology, The Netherlands; 2007.
[26] Lilliu G, van Mier JGM. On the relative use of micro-mechanical lattice analysis of 3-phase particle composites. Eng Fract Mech 2007;74:1174–89.
[27] Man H-K, van Mier JGM. Size effect on strength and fracture energy for numerical concrete with realistic aggregate shapes. Int J Fract 2008;154(1):61–72.
[28] Man H-K, van Mier JGM. Damage distribution and size effect in numerical concrete from lattice analysis. Cement Concrete Compos 2011;33(9):867–80.
[29] Nakamura H, Srisoros W, Yashiro R, Kunieda M. Time-dependent structural analysis considering mass transfer to evaluate deterioration processes of RC structures. J Adv Concrete Technol 2006;4:147–58.
[30] Okabe A, Boots B, Sugihara K, Chiu SN. Spatial tessellations: concepts and applications of Voronoi diagrams, 2nd ed. Wiley series in probability and mathematical statistics. England, John Wiley & Sons Ltd.; 2000.
[31] Ostoja-Starzewski M. Lattice models in micromechanics. Appl Mech Rev 2002;55(1):35–59.
[32] Otsuka K, Date H. Fracture process zone in concrete tension specimen. Eng Fract Mech 2000;65:111–31.
[33] Roelfstra PE, Sadouki H, Wittmann FH. Le béton numérique. Mater Struct 1987;18:327–35.
[34] Schlangen E, van Mier JGM. Experimental and numerical analysis of micromechanisms of fracture of cement-based composites. Cement Concrete Compos 1992;14:105–18.
[35] Schlangen E, Garboczi EJ. Fracture simulations of concrete using lattice models: computational aspects. Eng Fract Mech 1997;57:319–32.
[36] Slowik V, Hübner T, Schmidt M, Villmann B. Simulation of capillary shrinkage cracking in cement-like materials. Cement Concrete Compos 2009;31(7):461–9.
[37] Tajima K, Shirai N. Numerical prediction of crack width in reinforced concrete beams by particle model. In: Meschke G, de Borst R, Mang H, Bićanić N, editors. Computational modeling of concrete structures. London: Taylor & Francis Group; 2006. 221-230.
[38] van Mier JGM. Framework for a generalized four-stage fracture model of cement-based materials. Eng Fract Mech 2008;75:5072–86.
[39] van Mier JGM. Fracture processes of concrete: assessment of material parameters for fracture models, new directions in civil engineering. Boca Raton: CRC Press; 1997.
[40] Vervuurt A. Interface fracture in concrete, Ph.D. Thesis. Delft University of Technology, The Netherlands; 1997.
[41] Winslow DN, Cohen MD, Bentz DP, Snyder KA, Garboczi EJ. Percolation and pore structure in mortars and concrete. Cement Concrete Res 1994;24:25–37.
[42] Yip M, Mohle J, Bolander JE. Automated modeling of 3-D structural components using irregular lattices. Comput-Aided Civ Infrastruct Eng 2005;20(6):393–407.
[43] Yip M, Li Z, Liao B-S, Bolander JE. Irregular lattice models of fracture of multiphase particulate materials. Int J Fract 2006;140:113–24.